Computationally-Guided Synthetic Control over Pore Size in Isostructural Porous Organic Cages

A. G. Slater,[1†] P. S. Reiss,[1†] A. Pulido,[2] M. A. Little,[1] D. L. Holden,[1] L. Chen,[1] S. Y. Chong,[1] B. M. Alston,[1] R. Clowes,[1] M. Haranczyk,[3] M. E. Briggs,[1] T. Hasell,[1] G. M. Day[2*] and A. I. Cooper[1*]

[1] Department of Chemistry and Materials Innovation Factory, University of Liverpool, Crown Street, Liverpool L69 7ZD, United Kingdom; [2] School of Chemistry, University of Southampton, Highfield, Southampton SO17 1BJ, United Kingdom; 3 Computational Research Division, Lawrence Berkeley National Laboratory, Berkeley, California 94720, United States

[†] These authors contributed equally to this work.

ABSTRACT: The physical properties of 3-D porous solids are defined by their molecular geometry. Hence, precise control of pore size, pore shape, and pore connectivity are needed to tailor them for specific applications. However, for porous molecular crystals, the modification of pore size by adding pore-blocking groups can also affect crystal packing in an unpredictable way. This precludes strategies adopted for isoreticular metal-organic frameworks, where addition of a small group, such as a methyl group, does not affect the basic framework topology. Here, we narrow the pore size of cage molecule, **CC3**, in a systematic way by introducing methyl groups into the cage windows. Computational crystal structure prediction was used to anticipate the packing preferences of two homochiral methylated cages, **CC14**-*R* and **CC15**-*R*, and to assess the structure–energy landscape of a **CC15**-*R* binary co-crystal, designed such that both component cages could be directed to pack with a 3-D, interconnected pore structure. The experimental gas sorption properties of these three cage systems agree well with physical properties predicted by computational energy–structure–function maps.

Introduction

There has been much interest recently in porous materials based on discrete organic molecules[1–4] such as porous organic cages (POCs)[5–9]. Counter to expectations, these materials are now beginning to rival extended bonded frameworks, such as metal-organic frameworks (MOFs),[10] covalent-organic frameworks (COFs),[11] and organic polymer networks.[12] For example, the apparent Brunauer-Emmett-Teller surface area (SA_{BET}) achieved in molecular solids has reached remarkably high values of up to 3758 $m^2\ g^{-1}$.[8] Porous molecular materials have certain unique advantages: for example, unlike extended frameworks, they can be processed directly in solution to produce composite membranes.[13] The properties of these molecular materials can also be varied in a modular way by forming porous co-crystals that contain more than one molecule[14,15] and by using specific solvents to direct cage molecules into particular useful crystal packings.[16,17]

CC3-*R* is a homochiral POC with four triangular windows that crystallises with a 3-D diamondoid pore topology. This porous structure, **CC3**α, has been well-studied, both experimentally and computationally, and shape- and size-selective molecular separations have been demonstrated.[18–20] The ability to tailor the pore channel size in **CC3** is an attractive target because this could enable new or more selective separations. For instance, narrowing of the pore window size in **CC3** might allow selectivity for small guests, such as hydrogen (H_2), deuterium (D_2), and tritium (T_2), which diffuse unimpeded through the pore network of unmodified **CC3**α. Traditional molecular sieving is impractical for the separation of isotopes, but kinetic quantum sieving is possible at low temperatures in materials with sufficiently narrow pore diameters (PD) of less than 0.7 nm.[21] Zeolites,[22] porous carbons,[23] and metal-organic frameworks[24] have been shown to have selectivity for D_2 over H_2; achieving D_2/H_2 selectivity with a solution-processable porous molecular material could lead to new isotope separation membranes. We therefore targeted POCs with smaller pores than **CC3**α, but with retention of the same 3-D diamondoid pore topology.

The use of methyl groups to reduce pore size has been reported previously for both MOFs and COFs.[25–27] Mastalerz *et al.* also reported a series of O-alkylated [4+6] cages with different cavity sizes, but the crystal packing of the O-methylated cage was

found to be different from the unmethylated cage, and the other four alkylated analogues were not sufficiently crystalline to allow structure determination.[28] This highlights the significant difficulty in controlling the pore size of organic cages in an 'isoreticular' manner. Small changes to the cage building blocks will often result in significant changes to the solid-state crystal packing, thwarting attempts to produce isoreticular series of POCs, as observed with the four imine POCs, **CC1**–**CC4**.[29,30] This sensitivity of crystal packing to molecular functionality is a central challenge in molecular crystal engineering, extending beyond the specific example of porous molecular solids.

Here, we report a computationally guided strategy for fine-tuning the pore size in crystalline POC materials. Our approach involves the addition of methyl groups to a parent cage, **CC3**-*R*. Two methylated TFB precursors, 1,3,5-trimethyl-2,4,6-tris(formyl)benzene (Me_3TFB) and 1,3,5-triacetylbenzene (TAB), were used to form these **CC3**-*R* analogues, referred to here as **CC14**-*R* and **CC15**-*R*, respectively (**Scheme 1**). In **CC14**-*R* and **CC15**-*R*, the methyl groups narrow the dimension of the triangular cage windows compared to the parent cage, **CC3**-*R*. Since crystal packing for molecules is known to be sensitive to such small modifications, we used crystal structure prediction (CSP) to investigate the packing preferences of the cages. **CC14**-*R* was predicted to pack isostructurally with **CC3**α, while polymorphism was predicted to be likely for **CC15**-*R* because of the absence of a strongly preferred, low-energy packing motif. To overcome the lack of a stable diamondoid porous packing for **CC15**-*R*, CSP was used to investigate co-crystallisation of **CC15**-*R* with **CC3**-*S*; these calculations showed that the desired diamondoid pore network is the most stable packing for the heterochiral, quasiracemic co-crystal. The CSP landscapes were then transformed into energy–structure–function (ESF) maps of pore size for the static predicted crystal structures. To account for the effects on porosity of thermal fluctuations, including flexibility of the molecular geometry, molecular dynamics (MD) simulations were used to calculate the pore size reduction in the methylated systems. All predictions were confirmed experimentally, illustrating that computational guidance allows us to target and access porous organic crystals with systematic control over pore size.

Discussion

Synthesis of methylated CC3 derivatives

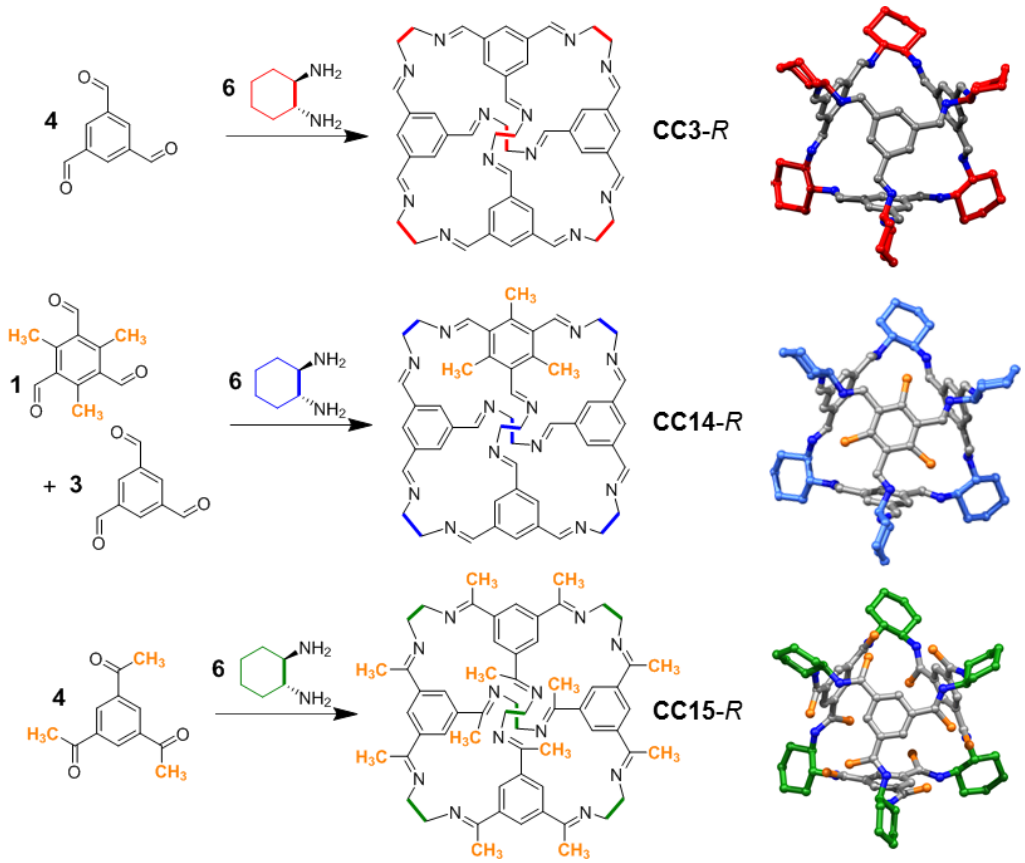

Scheme 1. Synthesis and schematic representation of cage molecules **CC3**-*R*, **CC14**-*R*, and **CC15**-*R*. The *S*-enantiomer would be formed from *S*,*S*-CHDA (not shown). In **CC14**-*R*, three of the four cage windows are partially occluded by a single methyl group per window (highlighted in orange), whereas in **CC15**-*R*, all four cage windows are partially occluded by three methyl groups per window (highlighted in yellow). Hydrogen atoms omitted for clarity.

We initially screened cage-forming reactions with methylated TFB precursors to determine whether **CC3**-*R* analogues could be synthesised. Me_3TFB (**Scheme 1**) was synthesised from 1,3,5-trimethyl-2,4,6-tris(bromomethyl)benzene *via* a modified Hass procedure.[31] Despite screening various conditions, a **CC3** derivative containing four Me_3TFB units per cage, an initial target of this study, could not be synthesised. This is most likely due to the steric hindrance of the methyl groups inhibiting the formation of a closed cage structure. Hence, different ratios of Me_3TFB and TFB were reacted with (*R*,*R*)-1,2-cyclohexanediamine (*R*,*R*-CHDA), and the product distribution was analysed by analytical high-performance liquid chromatography (HPLC). We showed previously that mixtures of POC molecules can be prepared by scrambling two vicinal diamines into the vertex positions of the cage.[32,33] In

those previous studies, all seven hypothetical scrambled cage species were obtained. By contrast, only two cage species were observed here—**CC3**-*R* and **CC14**-*R*, which has one Me_3TFB unit per cage—irrespective of the ratio of the two trialdehydes (**Table S1** and **Fig. S1**). **CC14**-*R* was isolated from this mixture of **CC3**-*R* and **CC14**-*R* in high purity using preparative HPLC (>99 % a/a by HPLC; **Fig. S2–7**).

To further occlude the cage windows, the methyl groups can be located on the imine such that they protrude further into the cage window. This was achieved by reacting TAB with *R*,*R*-CHDA to afford **CC15**-*R*, a **CC3**-*R* analogue with twelve methyl groups appended to the imine functionalities (**Scheme 1**, **Fig. S8–11**).

Crystal Structure Prediction and Energy-Structure-Function Maps

Crystal structure prediction (CSP) methods can determine the stable arrangements that are available to a molecule during crystallisation, as usually presented in plots of lattice energy versus crystal density or volume. The probability of a given structural arrangement being stable and experimentally accessible relates to its predicted lattice energy. Specific physical properties for each of the predicted structures, such as pore dimensionality, pore size, gas uptakes, and gas selectivity can also be calculated and projected onto CSP plots to create energy–structure–function (ESF) maps (**Fig. 1**).[34]

Previously, we used CSP to investigate the crystal packing preference of homochiral **CC3**-*R*;[14] the global lattice energy minimum predicted structure is the observed **CC3**α packing and is separated from the rest of the predicted structures by a large energy gap (**Fig. 1a,b**), indicating a strong thermodynamic preference for **CC3**-*R* to crystallize as **CC3**α (**Fig. 2e**).[29] Here, we used an equivalent computational strategy to investigate the crystal packing preferences of **CC14**-*R* and **CC15**-*R*. Starting points for the molecular geometries of **CC14**-*R* and **CC15**-*R* were obtained by adding methyl groups to the optimized gas phase geometry of **CC3**-*R*. The **CC14**-*R* and **CC15**-*R* isolated molecules were then geometry optimized using density functional theory (DFT) at the B3LYP/6-311G** level using the Gaussian09 software.[35] Molecular geometries were subsequently held rigid during crystal structure generation and lattice energy minimizations, which employed an anisotropic atom-atom potential using the DMACRYS software.[36]

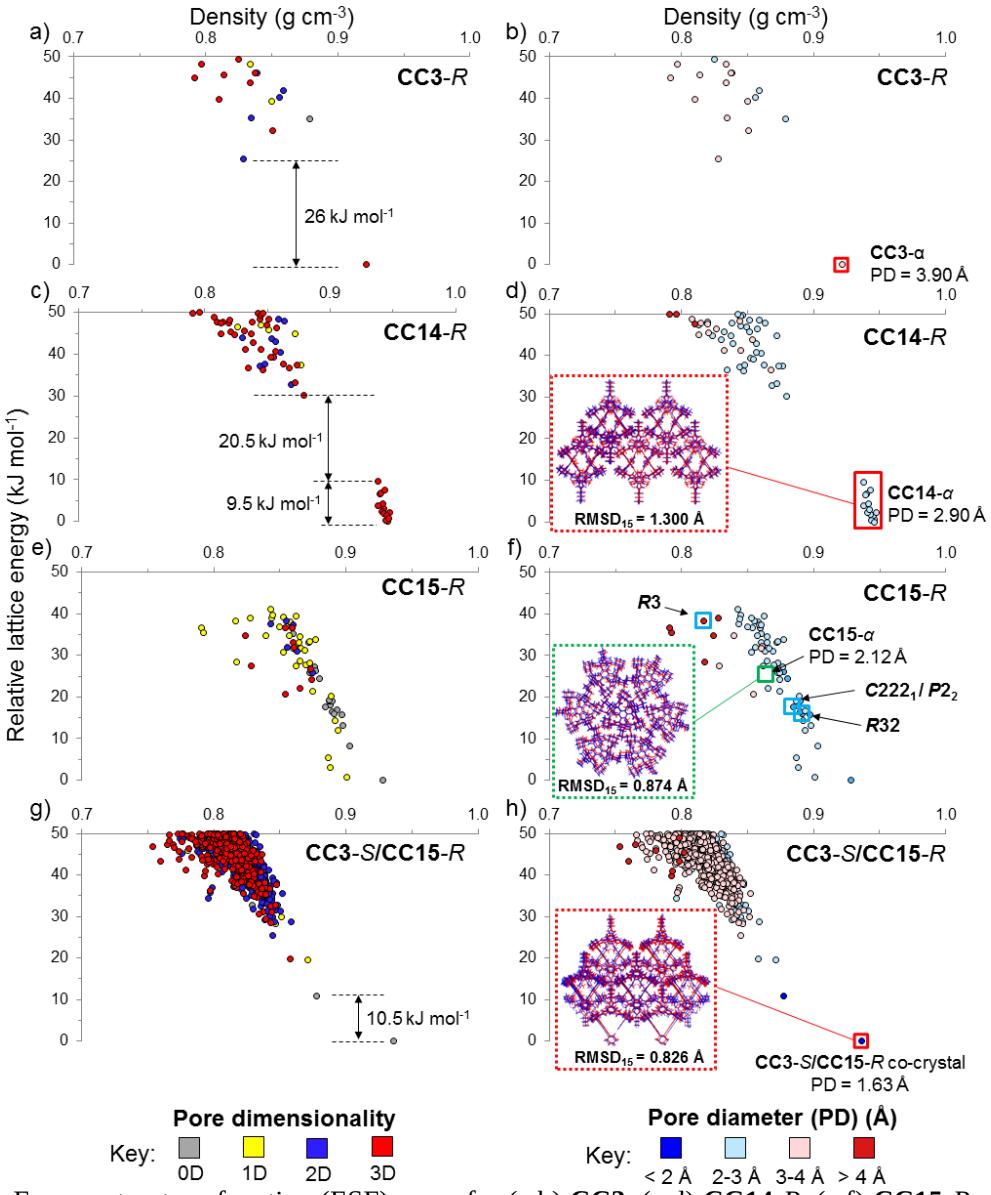

Figure 1. Energy-structure-function (ESF) maps for (a,b) **CC3,** (c,d) **CC14**-*R*, (e,f) **CC15**-*R*, and (g,h), the **CC3**-*S*/**CC15**-*R* co-crystal. Each point corresponds to a predicted crystal structure, color-coded by a calculated physical property. The symbols are color coded by (a,c,e,g) pore channel dimensionality, assessed using a H_2 probe radius (1.09 Å) or (b,d,f,h) by calculated pore diameter (PD). Despite having the desired window-to-window packing, the low energy predicted structures for the **CC3**-*S*/**CC15**-*R* co-crystals are 0D (non-porous) because the methyl groups occlude the pore to hydrogen, at least in the static crystal structure. All isolated, desolvated polymorphs that possess a diamondoid network are highlighted by a red square. For **CC15**-*R* (f), the green square highlights where the desolvated experimental structure would place on the landscape, while the blue squares highlight **CC15**-*R* structures that were observed experimentally as solvates (**c**). Insets show the overlay of molecular packing in experimentally determined (red) and calculated (blue) structures. $RMSD_{15}$ is the root mean squared deviation in atomic positions in the best overlay of a cluster of 15 molecules from the calculated and experimental structures, ignoring hydrogen atoms and disordered methyl groups for **CC14**. PD labelled on plots (b,d,f,h) is the calculated pore diameter.

In contrast to **CC3**-*R*, which has a unique predicted global minimum structure separated by 25.5 kJ mol^{-1} (**Fig. 1a,b**), the lattice energy landscape of homochiral **CC14**-*R* shows a cluster of fourteen structures, spread over an energy range of 9.5 kJ mol^{-1}, with a substantial gap of 20.5 kJ mol^{-1} between the top of this group and the rest of the energy landscape (**Fig. 1c,d**). All fourteen of these structures (**Fig. S12**) exhibit window-to-window packing and each possesses a diamondoid pore network that is isostructural with **CC3**α. The methyl groups are ordered in each of the 14 structures, but their relative orientation varies between structures. The small energy range encompassing this group of structures suggests that there might be no strong preference for the position of the methyl groups in the crystal. Hence, **CC14**-*R* is predicted to form a diamondoid porous network, like **CC3**α, where the cage molecules pack window-to-window, potentially with little preferential orientation and, thus, disorder of the methyl groups. That is, we can predict *a priori* that addition of three methyl groups to one aryl face of **CC3**-*R* should not disrupt its low energy packing mode.

For **CC15**-*R*, there are no large energy gaps between any of the low-energy predicted crystal structures (**Fig. 1e,f**), quite unlike the landscapes for **CC3**-*R* (**Fig. 1a,b**) and **CC14**-*R* (**Fig. 1c,d**). Even without detailed analysis of the structures in the landscape, this suggests that **CC15**-*R* lacks a strongly favoured packing mode and might have greater potential for polymorphism than either **CC3**-*R* or **CC14**-*R*. A search of this landscape shows that none of the predicted structures for **CC15**-*R* exhibits the desired diamondoid window-to-window packing up to at least 40 kJ mol^{-1} above the global minimum, which we estimate to be the energy window within which the CSP procedure used here has fully explored the range of possible structures. Therefore, window-to-window packing must be more than 40 kJ mol^{-1} less stable than the lowest energy predicted packing for this molecule. Rather than window-to-window packing, there is a predicted tendency for **CC15**-*R* to pack preferentially in a window-to-arene manner, which reduces pore connectivity in the crystal. To investigate the relative energy of the target diamondoid pore network, and to understand why it did not appear within the predicted structures, a computational model of **CC15**-*R* was built with the cages packed in the diamondoid window-to-window arrangement. Starting from the lowest energy predicted **CC3**α structure, **CC3**-*R* molecules were replaced with **CC15**-*R* and the generated structure was lattice energy minimized at the same level of theory used in the CSP calculations. This resulting isostructural **CC15**-*R* model structure (**Fig. S14a**) was predicted

to be 99 kJ mol^{-1} above the CSP global energy minimum (**Fig. S15**, black diamond) with a lattice energy of −120.8 kJ mol^{-1}. In this artificially produced structure, steric repulsion between the methyl groups forces the **CC15**-*R* molecules further apart (**Fig. S14**), resulting in a much lower crystal density of 0.676 g cm^{-3} (**Fig. S14–15**) compared to 0.922 g cm^{-3} for **CC3**α (**Table S2**). Even allowing for solvent stabilisation effects, which can stabilise lower-density crystal packings, these relative stabilities suggest that **CC15**-*R*, unlike **CC14**-*R*, should not form a phase that is isostructural with **CC3**α.

Previous studies[14,15,29] have shown that preferential heterochiral window-to-window interactions between opposite handed cages can favour window-to-window crystal packings. To investigate whether **CC15**-*R* would benefit from the additional stabilization brought by co-crystallizing cages of opposite chirality, we built computational models of racemic **CC15** (**CC15**-*S*/**CC15**-*R*) and the quasiracemic **CC3**-S/**CC15**-*R* co-crystal, following a similar strategy used for the window-to-window **CC15**-*R* model. The racemic **CC15** structure was approximately 26 kJ mol^{-1} more stable than the corresponding homochiral **CC15** model (**Table S2**), but the overall relative stability was still 73 kJ mol^{-1} above the global minimum homochiral structure (**Table S2** and **Fig. S15**), and hence energetically disfavoured. The extent of methylation in **CC15** seems to make a diamondoid, window-to-window packing mode unfavourable for both homochiral and racemic forms.

In principle, co-crystallisation of **CC15**-*R* with a structurally related cage without methyl groups, such as **CC3**-*S*, might reduce the steric repulsion between adjacent cages enough to allow window-to-window packing, while still allowing the methyl groups in **CC15** to constrict the diamondoid pore dimensions. CSP was therefore used to investigate packing preferences of **CC3**-*S*/**CC15**-*R* (**Fig. 1g,h**), assuming a 1:1 stoichiometry of **CC3**-*S* to **CC15**-*R*. The global lattice energy minimum predicted structure exhibits the desired **CC3**-S/**CC15**-*R* window-to-window arrangement (**Fig. 1h**, red square) and was separated by 10.8 kJ mol^{-1} from the remainder of predicted structures. Hence, these calculations demonstrate that co-crystallization with **CC3** should accommodate the 12 additional methyl groups in **CC15,** restoring the energetic preference for the desired diamondoid pore network.

Pore dimensionality was calculated for each structure in the four systems, using a 1.09 Å hydrogen probe radius (**Fig. 1a,c,e,g**). Both **CC3**-*R* and **CC14**-*R* show a high proportion of 3D pore networks (**Fig. 1a,c** filled red circles), whereas **CC15**-*R* exhibits a broader array of dimensionalities (**Fig. 1e**, filled grey, yellow, blue, and red circles). The latter can be attributed to the additional methyl groups in **CC15**-*R*, which frustrate the window-to-window packing between cages, as discussed above. Co-crystallization of **CC15**-*R* with **CC3**-*S* increases the proportion of structures that possess a 3D pore network (**Fig. 1g**, filled red circles), although unlike for **CC3**-*R* (**Fig. 1a**) and **CC14**-*R* (**Fig. 1c**), the global minimum structure is predicted to have 0D porosity with respect to the probe radius, despite having the desired window-to-window packing. This is due to the methyl groups in **CC15**-*R*, which narrow the pore window size in the static crystal structure. This is also apparent in the respective ESF maps for pore diameter (**Fig. 1b,d,h**), which predict that the pore diameter for the global minimum structure decreases, as denoted by the color-coding in these maps, in the isoreticular series **CC3**-*R* (**Fig. 1b**, pink circle) to **CC14**-*R* (**Fig. 1d**, light blue circles) to **CC3**-*S*/**CC15**-*R* (**Fig. 1h**, dark blue circle). The trend in the pore diameter goes **CC3α** (3.90 Å) > **CC14** (2.90 Å) > **CC3**-*S*/**CC15**-*R* co-crystal (1.63 Å), highlighting that the addition of methyl groups to the **CC3** core tunes pore size. Although there is a spread of low energy structures for **CC14**-*R* (**Fig. 1d**) the pore diameter for these are all equivalent.

Crystallization of methylated CC3 derivatives

Vial-in-vial crystallization of **CC14**-*R* from dichloromethane (DCM)-acetone gave octahedral crystals that were characterized by single crystal X-ray diffraction (SCXRD). **CC14**-*R* crystallized in the chiral cubic space group $F4_132$. As predicted by CSP, **CC14**-*R* packs isostructurally with **CC3**α to form **CC14**α (**Fig. 1d**; **2a,b,e,f** and **3a,b**). In **CC14**α, the cage has tetrahedral symmetry and packs window-to-window such that a diamondoid pore network passes though the cage windows. No ordering of the methyl groups between cages was apparent by experiment (**Fig. 2f** and **S16**), again in keeping with the CSP landscape for **CC14**-*R* (**Fig. 1c,d**). A bulk sample of **CC14**α was prepared by layering acetone onto a solution of the cage in DCM, followed by slow evaporation under a flow of nitrogen. This bulk material was desolvated at 60 °C under vacuum, and PXRD analysis confirmed that the desolvated **CC14**α matched the simulated powder pattern from the SCXRD (**Fig. S17**).

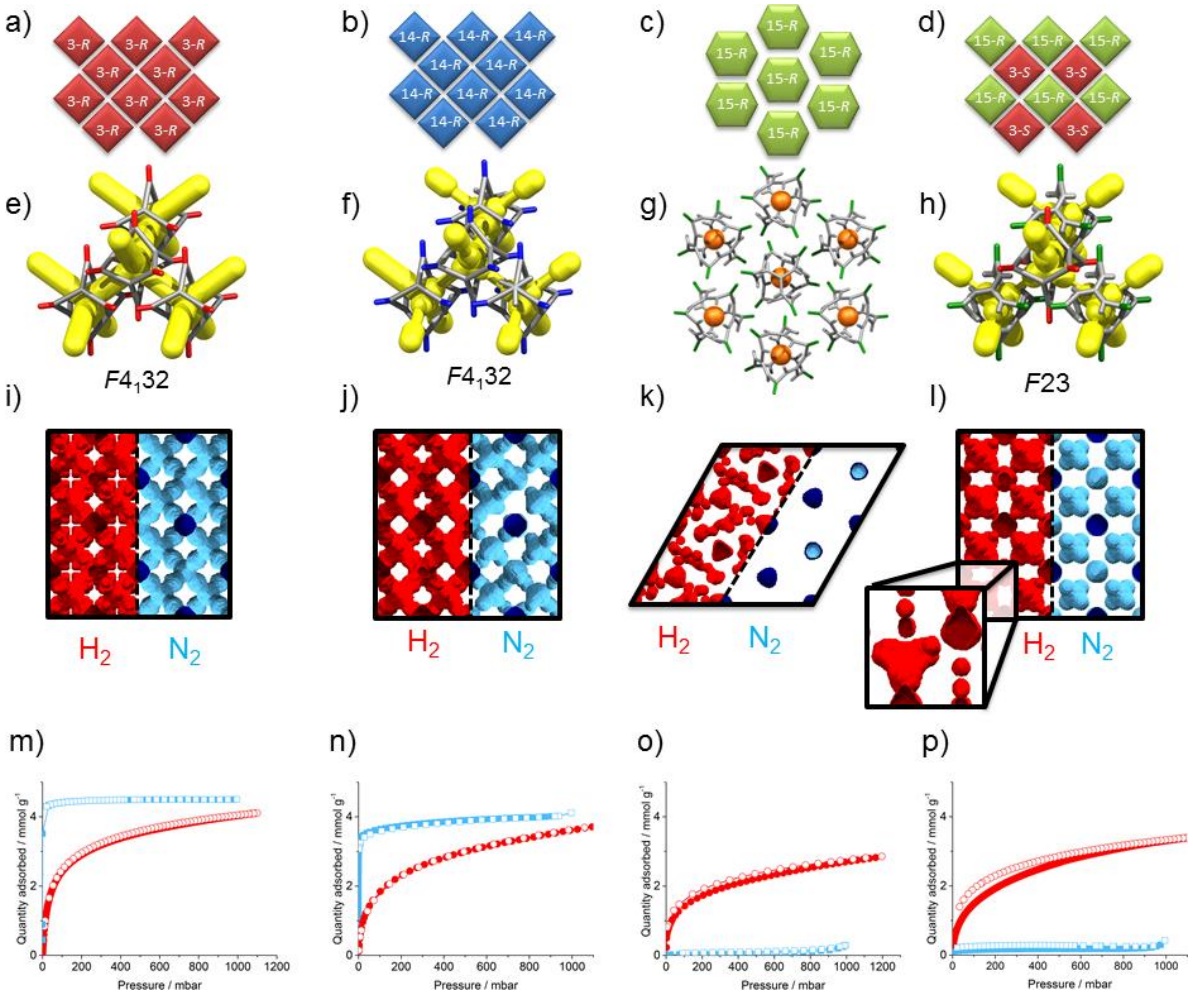

Figure 2. Crystal packing, pore topology, surface area plots, and sorption isotherms for homochiral **CC3**α, **CC14**α, **CC15**α, and **CC3**-*S*/**CC15**-*R* co-crystal. (a–d) Simplified representation of the cage packing in **CC3**α, **CC14**α, **CC15**α, and **CC3**-*S*/**CC15**-*R* co-crystal. (e–h) Simplified representation of the crystal structures of these cages, with pore channels shown in yellow. (i–l) Surface area plots, measured with two probe sizes; H_2 (red, 1.09 Å), the other N_2 (blue, 1.7 Å). As more methyl groups are added to the structures (from left to right), the pores become narrower; in **CC15**α and **CC3**-*S*/**CC15**-*R* co-crystal the cage cavities are occluded for a N_2 probe. These correlate well with the (m-p) hydrogen (red) and nitrogen (blue) sorption isotherms for **CC3**α, **CC14**α, **CC15**α, and **CC3**-*S*/**CC15**-*R* co-crystal respectively at 77 K and 1 bar. Closed symbols show adsorption and open symbols show desorption isotherms respectively.

A crystallisation screen of **CC15**-*R* identified various solvates, but as suggested by the CSP, we were unable to isolate any material that possessed a **CC3**α-like window-to-window packing. **CC15**-*R* crystallized from DCM-methanol in the trigonal space group *P*3 (with 3 independent molecules in the asymmetric unit, Z'=3) where **CC15**-*R* packs window-to-arene along *c* (**Fig. S19**), which was a common feature observed in

the CSP data set. A single crystal of the *P*3 structure was thermally desolvated *in situ* to yield **CC15**α (**Fig. 1f**, **2c,g** and **3c,d**). Desolvation was accompanied by a contraction in the cell volume (~ 9% at 100 K, equating to a contraction of ~ 206 $Å^3$ of the unit cell volume per **CC15**-*R*) because the window-to-arene stacks pack closer together along *a* and *b* (**Fig. S20**). Three additional solvated crystal structures were obtained in the space groups $C222_1$, *R*32, and *R*3 (**Fig. S21–25**, **Table S3**), respectively, with the orthorhombic $C222_1$ phase observed to undergo a single-crystal to single-crystal transformation to monoclinic $P2_1$ upon thermal desolvation (**Table S4**). A single window-to-window interaction was evident in the $C222_1$ and $P2_1$ crystal structures, at a cage centre to cage centre separation distance of approximately 12 Å; this is approximately 1 Å longer than the comparable distance in **CC3**α. Due to the absence of a preferential crystal packing motif, it proved difficult to obtain phase-pure samples for **CC15**-*R* on a large scale; again, this was suggested by the CSP landscape for this molecule (**Fig. 1e,f**). Only the trigonal *P*3 crystalline phase of **CC15**α could be isolated on a significant scale with sufficient phase purity. Desolvation of this bulk material at 100 °C for 12 hours was carried out with no apparent loss of crystallinity (**Fig. S26–27**), and the gas sorption properties of this desolvated material were investigated.

One current limitation of CSP is the huge computational expense of modelling high Z' structures, such as the *P*3, Z'=3 polymorph; with three crystallographically distinct **CC15** cages in the asymmetric unit. Sampling the full structural space for such low symmetry structures is computationally unaffordable within a reasonable timescale for this size of molecule, so this structure was not within the predicted set. By contrast, three of the other experimental **CC15** solvates (Z' = 1) were found among the set of predicted structures in space groups *C*2 (*R*32 solvate), $P2_1$ ($P2_1$ and $C222_1$ solvates), and *P*1 (*R*3 solvate), with relative energies of 16, 18, and 38 kJ mol^{-1}, respectively, above the global minimum (**Fig. 1f**, **Table S2** and **Fig. S13**). To calculate the relative stability of the observed experimental **CC15**α polymorph (Z' = 3), a computational model was built from the desolvated SCXRD data. Using this model, **CC15**α was found to be located 25 kJ mol^{-1} above the global minimum on the predicted **CC15**-*R* energy landscape (**Fig. 1f**, green square), and hence it has comparable relative stability to the other observed **CC15**-*R* solvates. As such, the formation of all four of these solvate structures can be ascribed to stabilising effect of the crystallization

solvents.[29,34,37] A good geometric match was observed between the observed **CC15**-*R* solvate frameworks and the predicted structures (**Fig. 1f** and **S13**).

We also attempted to crystallise **CC15**-*S* with **CC15**-*R* to see whether heterochiral cage pairings could direct window-to-window crystal packings, notwithstanding our calculations, above, which suggest that this should not succeed. When racemic **CC15** was crystallized from DCM-hexane or DCM-Et_2O, centrosymmetric $P\bar{1}$ and $P2_1/n$ crystal structures were isolated, respectively (**Fig. S29–30**). As predicted, neither structure displayed the desired window-to-window packing mode. By contrast, the **CC3**-*S*/**CC15**-*R* co-crystal was successfully prepared by mixing a solution of **CC15**-*R* with an equimolar quantity of **CC3**-*S* in DCM. A homogeneous, clear solution was produced; this turned cloudy after standing for 1 hour as crystallites were formed. Structure determination by SCXRD revealed the diamondoid **CC3**-*S*/**CC15**-*R* co-crystal in the chiral cubic space group *F*23, which was the only polymorph isolated in these experiments. In agreement with the CSP global lattice energy minimum, the cage molecules pack window-to-window (**Fig. 1h**), with each **CC3**-*S* cage surrounded by four **CC15**-*R* cages (**Figs. 2d,h** and **S31**). PXRD analysis of the desolvated bulk material showed that it remained phase-pure and matched the simulated data from the single crystal (**Fig. S32**).

Computational investigation of physical properties

Computed ESF maps (**Fig. 1b,d,h**) give us an *a priori* picture of the likely decrease in the pore diameter for the isoreticular series **CC3**α – **CC14**α – **CC3**-*S*/**CC15**-*R* co-crystal. However, these ESF maps are produced from static predicted crystal structures: they do not take account of the effect of lattice vibrations on pore dimensions and connectivity. In previous studies,[38–40] molecular dynamics (MD) simulations were used to understand the diffusivity of small gas molecules in **CC3**α and to calculate a time-averaged, pore-limiting envelope (PLE), which accounts for molecular motion about the equilibrium crystal structure, as well as molecular flexibility and intramolecular vibrations. This PLE rationalizes the diffusion of gas molecules such as Kr, Xe, and SF_6, which have kinetic diameters that are larger than the pore diameter for **CC3**α.[19,41] Here, we used MD calculations to evaluate the properties of our isoreticular series of cage co-crystals, and to investigate the effect of

the methyl groups on both the cavity size and on the PLE. For reasons of computational expense, these MD simulations were carried out for individual structures, but in principle this could be automated to produce dynamic PLE ESF maps, analogous to the static PD ESF maps shown in **Fig. 1b,d,f,h**.

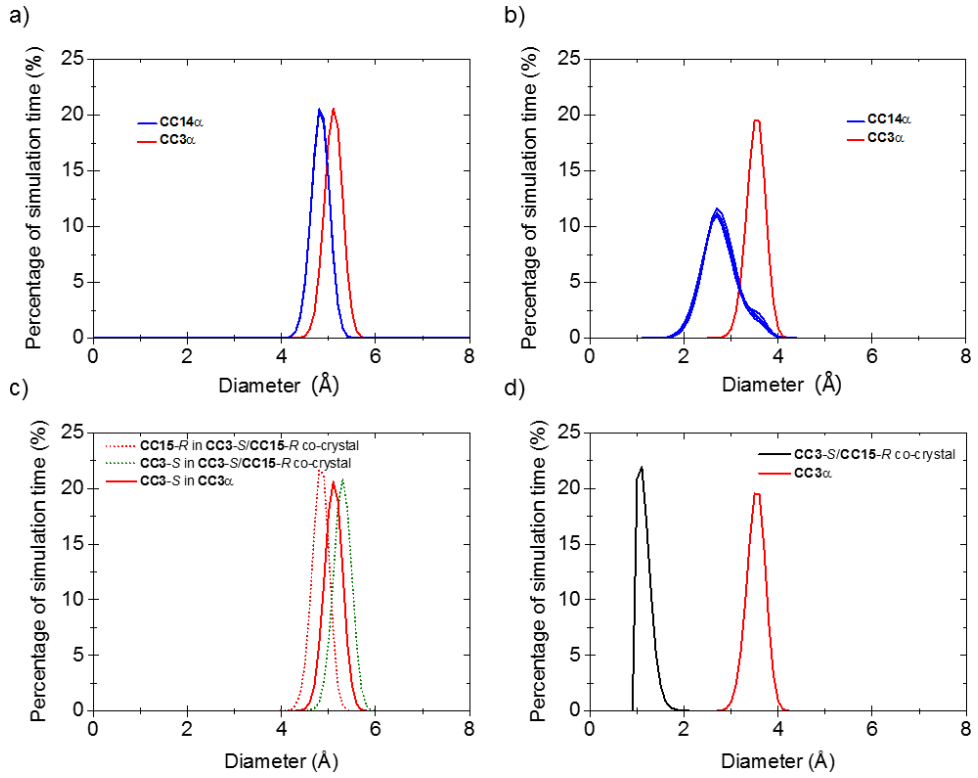

Figure 3. (a, b) Overlaid analysis for five different models of the **CC14**α crystal structure showing (a) the cage cavity size, and (b) PLE. The cage cavity size distribution and PLE for **CC3**α are shown in red for comparison. (c) Cage cavity size distribution and (d) PLE for the predicted **CC3**-*S*/**CC15**-*R* co-crystal. **CC3**α is shown in red for comparison.

For **CC14**-*R*, the position of the methylated benzene is disordered with respect to adjacent cage molecules. MD simulations were therefore run for five structural models with the methylated benzene placement randomised to ensure that a statistical representation of different packing motifs was sampled. Analysis of the five simulated **CC14**-*R* structures showed that the cavity size distribution for all five models remained consistent, even though the position of the methylated benzene was randomized — this was confirmed by the visual pore size distribution plots (**Fig. S34**). This resulted in a slightly reduced average cavity size of 4.80 Å (the peak of the cage size distribution), as compared with 5.10 Å in **CC3**-*R* (**Fig. 3a**). As expected, the PLE of **CC14**-*R* was reduced, with the precise shape of the pore envelope determined by the relative positions of the methylated cage windows of adjacent cages in the five

CC14-*R* simulations. This is reflected by the variation in intensity in the shoulder peak of the PLE for the different models **(Fig. 3b)**. The surface area plots (**Fig. 2j** and **S34**) also show that the methyl groups in **CC14**-*R* have a direct impact on the interstitial void sites in the structure with respect to **CC3**. When compared to both homochiral and racemic **CC3**α, the size of these interstitial sites in **CC14**-*R* is reduced from ~2.50 Å to 1.5–2.0 Å. This creates a bottleneck in the structure, which could directly impact the diffusion kinetics of gases.

For the **CC3**-*S*/**CC15**-*R* co-crystal, the PLE is restricted by the three ordered methyl groups in each **CC15**-*R* window. These groups reduce the PLE dramatically, shifting the most probable window size from 3.60 Å (for **CC3**-*R*) to just 1.09 Å (**Fig. 3d**). Thus, the N_2 surface area plot (**Figs. 2l**) shows disconnected cage cavities. Taken alone, this would suggest that the cage window in this co-crystal is too small for any gas diffusion, even for H_2. However, the PLE was calculated using the empty, guest-free cage structure, which does not account for the possibility of cooperative diffusion.[42] Analysis of the cavity size distribution for the **CC3**-*S*/**CC15**-*R* co-crystal shows that there are two distinct cavity sites arising from the two different cages in the co-crystal (**Fig. 3c**). Interestingly, the cavity size for **CC3**-*S* in the **CC3**-*S*/**CC15**-*R* co-crystal is smaller than it is in homochiral **CC3**α, with an average diameter of 4.80 Å versus 5.10 Å in homochiral **CC3** (black vs red curves, respectively in **Fig. 3c**). This is nearly identical to the cage cavity size in **CC14**-*R* (black curve, **Fig. 3a**). **CC15**-*R* in this co-crystal has the largest internal cavity in this isoreticular cage series, with an average diameter of 5.30 Å (blue curve, **Fig. 3c**).

Experimental Gas Sorption Properties

This isoreticular cage series allows us to evaluate the effect of pore size reduction on gas uptakes and diffusion kinetics (**Figure 2m-p**, **Table 1**). Nitrogen sorption measurements for **CC14**α at 77 K and 1 bar displayed a Type I isotherm, as rationalized by the crystal structure, which mirrors the isotherm shape of **CC3**α (**Fig. 2m,n** and **S35**). The overall nitrogen uptake and apparent BET surface area for **CC14**α (4.11 mmol g^{-1}, 320 m^2 g^{-1}) are slightly lower than for **CC3**α (4.50 mmol g^{-1}, 409 m^2 g^{-1}).[38] This decrease in specific surface area and gas uptake can be explained by the reduction in pore volume associated with the introduction of the methyl groups and the accompanying increase in molecular mass of the cage — these also block off

some of the pore channels (**Fig 2j)**. The sorption properties of this material with respect to other gases (H_2, CO_2, Xe, Kr) followed a similar trend, with slightly lower uptakes than for **CC3**α in each case (**Fig. S35**–**36**). The pore-size distribution (PSD) of these two cages, measured using CO_2 as a probe gas (**Fig. S37**), shows a moderate decrease in pore width after introduction of the methyl groups, as suggested by the predicted PLE plots (**Fig. 3a**). **CC14**α has a similar sorption selectivity to **CC3**α for Xe over Kr.[19]

Table 1. Comparison of the gas uptakes at 1 bar for **CC3**α, **CC14**α, **CC15**α, and quasiracemate **CC3**-*S*/**CC15**--*R*.

	SA_{BET} / $m^2\ g^{-1}$	N_2 / mmol g^{-1}	H_2 / mmol g^{-1}	CO_2 / mmol g^{-1}	Xe / mmol g^{-1}	Kr / mmol g^{-1}
	77 K	77 K	77 K	273 K	273 K	273 K
CC3α	409	4.50	5.00	2.01	2.60	1.52
CC14α	320	4.11	3.64	1.57	1.61	0.96
CC15α	2.7	0.29	2.85	1.30	1.14	0.81
CC3-*S*/**CC15**-*R* co-crystal	13.1	0.43	3.39	1.84	1.25	0.79

Nitrogen sorption measurements for **CC15**α at 77 K and 1 bar showed very little gas uptake in comparison to **CC3**α. This highlights that the twelve methyl groups on each cage affect both the crystal packing of **CC15**α and accessibility to the intrinsic cage voids, effectively shutting out nitrogen from the pores at 77 K (**Table 1** and **Fig. S38**). By contrast, **CC15**α adsorbs approximately half as much H_2 and CO_2 in comparison to **CC3**α, illustrating both a degree of porosity to smaller gas molecules at 77 K and increased flexibility at higher temperatures, respectively (**Fig. S38**–**39**).

Gas sorption isotherms for the **CC3**-*S*/**CC15**-*R* co-crystal showed it to be non-porous to nitrogen at 77 K (**Fig. 2p** and **S40**), confirming that the three methyl groups in each **CC15**-*R* window narrow the pore network in the crystal substantially. This material

was, however, porous to H_2 at 77 K (**Fig. 2p** and **S40**), with only a slight reduction in uptake compared to **CC3**α, attributable to the reduced pore volume and increased average cage mass. However, there was a notable hysteresis in the H_2 isotherm, most likely due to slower kinetics (**Fig. 2p**). Despite its narrower pore channels, this structural analogue of **CC3**α remains porous to CO_2 and Xe at higher temperatures (**Fig. S41–42)**, again illustrating the important role that molecular flexibility and cooperative diffusion plays in defining the properties of these porous materials and suggesting that the methyl groups in the windows act like a 'saloon door' (**Fig. S43-44**).[43] This would explain the observed xenon uptake (Xe diameter = 4.10 Å) in the co-crystal, albeit with a pronounced hysteresis on desorption that is not observed for the isostructural **CC3**α, indicating of slower kinetics (**Fig. S42**). Controlling the diffusion of Xe through the cage crystals in this way might give practical advantages in terms of breakthrough separations, with relevance to the treatment of radioactive air streams.[44] Narrow pore structures, such as those found in the **CC3**-*S*/**CC15**-*R* co-crystal, could also hold promise for isotope separation by quantum sieving. We believe that the narrow-pore **CC3**-*S*/**CC15**-*R* co-crystal could have a potential for separating mixtures of H_2 and D_2, exploiting both kinetic and thermodynamic aspects of the quantum sieving effect (**Fig. S45-46**).

Conclusions

The methylation of TFB was chosen as a strategy to narrow the dimensions of the windows in analogues of the porous organic cage **CC3**, with the aim of inducing selectivity in the resultant porous materials. Two novel methylated organic cages, **CC14**-*R* and **CC15**-*R*, were prepared. CSP was used to investigate the effect on cage packing preferences that are induced by window methylation, and hence to guide the design of pore-narrowed isoreticular networks using ESF maps to visualize the impact on physical properties. In agreement with the CSP, **CC14**-*R* adopts the window-to-window packing analogous with **CC3**α, whereas **CC15**-*R* prefers to pack in a window-to-arene configuration, unless it is co-crystallized with a less bulky co-former, **CC3**-*S*. This illustrates the value of CSP in the design of functional materials: the introduction of methyl groups in **CC14**-*R* is innocuous with respect to diamondoid crystal packing whereas in **CC15**-*R* it is not, illustrating the limitations of intuitive crystal engineering strategies. The timescale for the single component CSP calculations (approximately 83,000 CPU hours, or 7 to 10 days in real time) is competitive with experimental timescales for synthesis and characterization of these materials, and this timescale is set to be reduced substantially as computational hardware and CSP methods evolve in the future. This should make it feasible, for example, to make routine *a priori* searches for more complex structures, such as those with multiple independent molecules including co-crystals and higher Z' structures, such as **CC15**α.

In the future, we envisage combined computational and experimental design strategies that build on these findings, such as investigating the potential effect of fluorination of the methyl groups. This could lead to a broader family of cages with tuneable properties for specific applications. Our observations also raise the question of how to maintain selectivity while increasing the adsorption capacity of the material. One possible strategy is to adapt the principles demonstrated here for related molecules, such as **CC9** and **CC10**, where the vertex groups were chosen to direct molecular assembly and to create additional, extrinsic porosity.[45] Large extrinsic pores interconnected by narrow intrinsic pore bottlenecks could lead to high capacity materials with good adsorption/desorption kinetics and tuneable guest selectivity.

Acknowledgements

We acknowledge the Engineering and Physical Sciences Research Council (EP/N004884/1) and European Research Council under the European Union's Seventh Framework Programme (FP/2007-2013) through grant agreement numbers 321156 (ERC-AG-PE5-ROBOT) and 307358 (ERC-stG-2012-ANGLE) for funding. AGS thanks the Royal Society for a Dorothy Hodgkin Fellowship. T.H. thanks the Royal Society for a University Research Fellowship. We thank Diamond Light Source for access to beamlines I19 (MT11231) and I11 (EE12336) that contributed to the work here. We thank the Advanced Light Source, supported by the Director, Office of Science, Office of Basic Energy Sciences, of the US Department of Energy under contract number DE-AC02-05CH11231, and S. J. Teat and K. J. Gagnon for their assistance. We acknowledge the ARCHER UK National Supercomputing Service via an EPSRC Programme Grant (EP/N004884), and the use of the IRIDIS High Performance Computing Facility, and associated support services at the University of Southampton, in the completion of this work.

References

(1) Zhang, G.; Mastalerz, M. *Chem. Soc. Rev.* **2014**, 43, 1934.

(2) Tian, J.; Thallapally, P. K.; McGrail, B. P. *CrystEngComm* **2012**, 14, 1909.

(3) Mastalerz, M. *Angew. Chem. Int. Ed.* **2010**, 49, 5042.

(4) Slater, A. G.; Cooper, A. I. *Science* **2015**, 348, 8075.

(5) Tozawa, T.; Jones, J. T. A; Swamy, S. I.; Jiang, S.; Adams, D. J.; Shakespeare, S.; Clowes, R.; Bradshaw, D.; Hasell, T.; Chong, S. Y.; Tang, C.; Thompson, S.; Parker, J.; Trewin, A.; Bacsa, J.; Slawin, A. M. Z.; Steiner, A.; Cooper, A. I. *Nat. Mater.* **2009**, 8, 973.

(6) Mastalerz, M.; Schneider, M. W.; Oppel, I. M.; Presly, O. *Angew. Chem. Int. Ed.* **2011**, 50, 1046.

(7) Hong, S.; Rohman, M. R.; Jia, J.; Kim, Y. Y.; Moon, D.; Kim, Y. Y.; Ko, Y. H.; Lee, E.; Kim, K. *Angew. Chem. Int. Ed.* **2015**, 54, 13241.

(8) Zhang, G.; Presly, O.; White, F.; Oppel, I. M.; Mastalerz, M. *Angew. Chem. Int. Ed.* **2014**, 53, 1516.

(9) Avellaneda, A.; Valente, P.; Burgun, A.; Evans, J. D.; Markwell-Heys, A. W.; Rankine, D.; Nielsen, D. J.; Hill, M. R.; Sumby, C. J.; Doonan, C. J. *Angew. Chem. Int. Ed.* **2013**, 52, 3746.

(10) Yaghi, O. M.; Li, H.; Davis, C.; Richardson, D.; Groy, T. L. *Acc. Chem. Res.* **1998**, 31, 474.

(11) Côté, A. P.; Benin, A. I.; Ockwig, N. W.; O'Keeffe, M.; Matzger, A. J.; Yaghi, O. M. *Science* **2005**, 310, 1166.

(12) Jiang, J. X.; Su, F.; Trewin, A.; Wood, C. D.; Campbell, N. L.; Niu, H.; Dickinson, C.; Ganin, A. Y.; Rosseinsky, M. J.; Khimyak, Y. Z.; Cooper, A. I. *Angew. Chem. Int. Ed.* **2007**, 46, 8574.

(13) Bushell, A. F.; Budd, P. M.; Attfield, M. P.; Jones, J. T. A.; Hasell, T.; Cooper, A. I.; Bernardo, P.; Bazzarelli, F.; Clarizia, G.; Jansen, J. C. *Angew. Chem. Int. Ed.* **2013**, 52, 1253.

(14) Jones, J. T. A.; Hasell, T.; Wu, X.; Bacsa, J.; Jelfs, K. E.; Schmidtmann, M.; Chong, S. Y.; Adams, D. J.; Trewin, A.; Schiffman, F.; Cora, F.; Slater, B.; Steiner, A.; Day, G. M.; Cooper, A. I. *Nature* **2011**, 474, 367.

(15) Hasell, T.; Chong, S. Y.; Schmidtmann, M.; Adams, D. J.; Cooper, A. I. *Angew. Chem. Int. Ed.* **2012**, 51, 7154.

(16) Hasell, T.; Culshaw, J. L.; Chong, S. Y.; Schmidtmann, M.; Little, M. A.; Jelfs, K. E.; Pyzer-Knapp, E. O.; Shepherd, H.; Adams, D. J.; Day, G. M.; Cooper, A. I. *J. Am. Chem. Soc.* **2014**, 136, 1438.

(17) Little, M. A.; Chong, S. Y.; Schmidtmann, M.; Hasell, T.; Cooper, A. I. *Chem. Commun.* **2014**, 50, 9465.

(18) Kewley, A.; Stephenson, A.; Chen, L.; Briggs, M. E.; Hasell, T.; Cooper, A. I. *Chem. Mater.* **2015**, 27, 3207.

(19) Chen, L.; Reiss, P. S.; Chong, S. Y.; Holden, D.; Jelfs, K. E.; Hasell, T.; Little, M. A; Kewley, A.; Briggs, M. E.; Stephenson, A.; Thomas, K. M.; Armstrong, J. a; Bell, J.; Busto, J.; Noel, R.; Liu, J.; Strachan, D. M.; Thallapally, P. K.; Cooper, A. I. *Nat. Mater.* **2014**, 13, 954.

(20) Mitra, T.; Jelfs, K. E.; Schmidtmann, M.; Ahmed, A.; Chong, S. Y.; Adams, D. J.; Cooper, A. I. *Nat. Chem.* **2013**, 5, 276.

(21) Cai, J.; Xing, Y.; Zhao, X. *RSC Adv.* **2012**, 2, 8579.

(22) Kowalczyk, P.; Terzyk, A. P.; Gauden, P. A.; Furmaniak, S.; Pantatosaki, E.; Papadopoulos, G. K. *J. Phys. Chem. C* **2015**, 119, 15373.

(23) Niimura, S.; Fujimori, T.; Minami, D.; Hattori, Y.; Abrams, L.; Corbin, D.; Hata, K.; Kaneko, K. *J. Am. Chem. Soc.* **2012**, 134, 18483.

(24) Oh, H.; Hirscher, M. *Eur. J. Inorg. Chem.* **2016**, 4278.

(25) Tilford, R. W.; Mugavero, S. J.; Pellechia, P. J.; Lavigne, J. *J. Adv. Mater.* **2008**, 20, 2741.

(26) Wang, Y.; Tan, C.; Sun, Z.; Xue, Z.; Zhu, Q.; Shen, C.; Wen, Y.; Hu, S.; Wang, Y.; Sheng, T.; Wu, X. *Chem. - A Eur. J.* **2014**, 20, 1341.

(27) Bhattacharya, B.; Haldar, R.; Dey, R.; Maji, T. K.; Ghoshal, D. *Dalton Trans.* **2013**, 43, 2272.

(28) Schneider, M. W.; Oppel, I. M.; Ott, H.; Lechner, L. G.; Hauswald, H. J. S.; Stoll, R.; Mastalerz, M. *Chem. - A Eur. J.* **2012**, 18, 836.

(29) Pyzer-Knapp, E. O.; Thompson, H. P. G.; Schiffmann, F.; Jelfs, K. E.; Chong, S. Y.; Little, M. a.; Cooper, A. I.; Day, G. M. *Chem. Sci.* **2014**, 5, 2235.

(30) Eddaoudi, M.; Kim, J.; Rosi, N.; Vodak, D.; Wachter, J.; O'Keeffe, M.; Yaghi, O. M. *Science* **2002**, 295, 469.

(31) Hass, H. B.; Bender, M. L. *Org. Synth.* **1950**, 30, 99.

(32) Jiang, S.; Jones, J. T. A; Hasell, T.; Blythe, C. E.; Adams, D. J.; Trewin, A.; Cooper, A. I. *Nat. Commun.* **2011**, 2, 207.

(33) Briggs, M. E.; Slater, A. G.; Lunt, N.; Jiang, S.; Little, M. A.; Greenaway, R. L.; Hasell, T.; Battilocchio, C.; Ley, S. V.; Cooper, A. I. *Chem. Commun.* **2015**, 51, 17390.

(34) Pulido, A.; Chen, L.; Kaczorowski, T.; Holden, D.; Little, M. A.; Chong, S. Y.; Slater, B. J.; McMahon, D. P.; Bonillo, B.; Stackhouse, C. J.; Stephenson, A.; Kane, C. M.; Clowes, R.; Hasell, T.; Cooper, A. I.; Day, G. M. *Nature* **2017**, 543, 657.

(35) Frisch, M. J.; Trucks, G. W.; Schlegel, H. B.; Scuseria, G. E.; Robb, M. A.; Cheeseman, J.R; Scalmani, G.; Barone, V.; Mennucci, B.; Petersson, G. A.; Nakatsuji, H.; Caricato, M.; Li, X.; Hratchian, H. P.; Izmaylov, A. F.; Bloino, J.; Zheng, G.; Sonnenberg, J. L.; Hada, M.; Ehara, M.; Toyota, K.; Fukuda, R.; Hasegawa, J.; Ishida, M.; Nakajima, T.,;

Honda, Y.; Kitao, O.; Nakai, H.; Vreven, T.; Montgomery Jr., J. A.; Peralta, J. E.; Ogliaro, F.; Bearpark, M.; Heyd, J. J.; Brothers, E.; Kudin, K. N.; Staroverov, V. N.; Kobayashi, R,; Normand, J.; Raghavachari, K.; Rendell, A.; Burant, J. C.; Iyengar, S. S.; Tomasi, J. Cossi, M.; Rega, N.; Millam, J. M.; Klene, M.; Knox, J. E.; Cross, J. B.; Bakken, V.; Adamo, C.; Jaramillo, J.; Gomperts, R.; Stratmann, R. E.; Yazyev, O.; Austin, A. J.; Cammi, R.; Pomelli, C.; Ochterski, J. W.; Martin, R. L.; Morokuma, K.; Zakrzewski, V. G.; Voth, G. A.; Salvador, P.; Dannenberg, J. J.; Dapprich, S.; Daniels, A. D.; Farkas, Ö.; Foresman, J. B.; Ortiz, J. V.; Cioslowski, J.; Fox, D. J. Gaussian 09, Revision D.01, Gaussian, Inc., Wallingford CT, **2009**.

(36) Price, S. L.; Leslie, M.; Welch, G. W. A.; Habgood, M.; Price, L. S.; Karamertzanis, P. G.; Day, G. M. *Phys. Chem. Chem. Phys.* **2010**, 12, 8478.

(37) Cruz-Cabeza, A. J.; Day, G. M.; Jones, W. *Chem. - A Eur. J.* **2009**, 15, 13033.

(38) Holden, D.; Jelfs, K. E.; Cooper, A. I.; Trewin, A.; Willock, D. J. *J. Phys. Chem. C* **2012**, 116, 16639.

(39) Camp, J. S.; Sholl, D. S. *J. Phys. Chem. C* **2016**, 120, 1110.

(40) Evans, J. D.; Huang, D. M.; Hill, M. R.; Sumby, C. J.; Thornton, A. W.; Doonan, C. J. *J. Phys. Chem. C* **2014**, 118, 1523.

(41) Hasell, T.; Miklitz, M.; Stephenson, A.; Little, M. A.; Chong, S. Y.; Clowes, R.; Chen, L.; Holden, D.; Tribello, G. A.; Jelfs, K. E.; Cooper, A. I. *J. Am. Chem. Soc.* **2016**, 138, 1653.

(42) Holden, D.; Chong, S. Y.; Chen, L.; Jelfs, K. E.; Hasell, T.; Cooper, A. I. *Chem. Sci*. **2016**, 7, 4875

(43) Fairen-Jimenez, D.; Moggach, S. A.; Wharmby, M. T.; Wright, P. A.; Parsons, S.; Düren, T. *J. Am. Chem. Soc.* **2011**, 133, 8900.

(44) Liu, J.; Thallapally, P. K.; Strachan, D. *Langmuir* **2012**, 28, 11584.

(45) Bojdys, M. J.; Briggs, M. E.; Jones, J. T. A.; Adams, D. J.; Chong, S. Y.; Schmidtmann, M.; Cooper, A. I. *J. Am. Chem. Soc.* **2011**, 133, 16566.

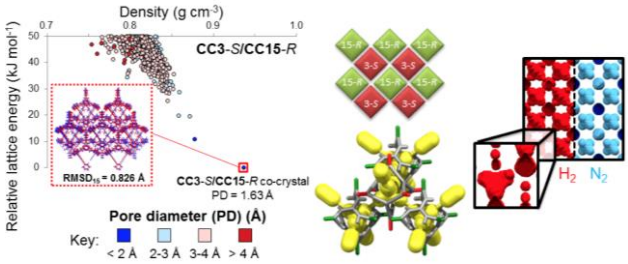

For Table of Contents Use Only: Computationally-Guided Synthetic Control over Pore Size in Isostructural Porous Organic Cages. A. G. Slater, P. S. Reiss, A. Pulido, M. A. Little, D. L. Holden, L. Chen, S. Y. Chong, B. M. Alston, R. Clowes, M. Haranczyk, M. E. Briggs, T. Hasell, G. M. Day* and A. I. Cooper*